Effect of welding heat input conditions on the dynamic behavior of pulse laser beam welding molten pool for Ti6Al4V thin plate with clearance

Bin Kong
Yanhong Wei
Fengye Tang
Yiting Chang
Jicheng Chen (chenjicheng1990@163.com)
Nanjing University of Aeronautics and Astronautics

Research Article

Keywords: Pulse laser beam welding, Ti6Al4V alloy plate, Laser peak power, Welding speed, Molten pool dynamic behavior

Posted Date: September 23rd, 2022

DOI: https://doi.org/10.21203/rs.3.rs-2069523/v1

Effect of welding heat input conditions on the dynamic behavior of pulse laser beam welding molten pool for Ti6Al4V thin plate with clearance

Bin Kong, Yanhong Wei, Fengye Tang, Yiting Chang, Jicheng Chen*

College of Material Science and Technology, Nanjing University of Aeronautics and Astronautics, Nanjing 210016, China

* *Corresponding author.*

E-mail address: chenjicheng1990@163.com (Jicheng Chen).

Abstract: For a practical pulse laser beam welding (PLBW) process of metal sheets assembled in butt joint configuration, the precise control of the assembling clearance has been a challenge. The existence of machining burrs and assembly errors will lead to forming severe defects, such as misalignment, welding leakage, and penetrating. In this paper, a pair of Ti6Al4V plates with a 0.2 mm air gap was tested by an improved PLBW process. A three-dimensional multi-phase and multi-physical field coupling model of Ti6Al4V alloy plate with a reserved air gap was established according to the weld profile, and the dynamic behavior of the keyhole and molten pool was simulated. Transient temperature field, velocity field, keyhole size, and liquid bridge connection were calculated by using different welding heat input parameters. The results showed that the weld profile simulated by the CFD model is in good agreement with the experimental results, and the deviation is between 0.68% and 7.95%. After the laser power reaches the peak value, the metal steam eruption weakens and the obvious Marangoni vortex appears in the molten pool. The simulated keyhole is always in three stages, that is, the keyhole appears, and then gradually forms the through-hole. The through hole keeps oscillating, and finally, the keyhole shrinks and disappears when the laser power drops to zero. With the increase of laser peak power, the keyhole shape becomes more curved, indicating that the keyhole oscillation is enhanced. With the increase in welding speed, the stability of the molten pool is improved, and the area of the liquid bridge rises more regularly.

Keywords: Pulse laser beam welding; Ti6Al4V alloy plate; Laser peak power; Welding speed; Molten pool dynamic behavior

1. Introduction

As we all know, titanium alloy is widely used in aerospace, medical field, material field, and petrochemical field. Ti6Al4V is the most commonly used among all titanium alloys because of its low density, high specific strength, and corrosion resistance [1]. However, it has the disadvantages of high melting temperature, low thermal conductivity, and easy oxidation during processing, which is not compatible with the traditional process [2]. The inherent material characteristics of Ti6Al4V alloy put forward stricter requirements on welding conditions.

Among many welding technologies, laser welding recently gained popularity as a promising joining technology for Ti6Al4V in industries because of its high weld quality, high precision, high efficiency, excellent flexibility, and low deformation. According to the consistency of the output energy, laser beam welding can be

split into two types: pulse laser beam welding (PLBW) and continuous laser beam welding (CLBW). The PLBW can be thought of as a combination of numerous single-spot welding. The laser irradiates the metal material for a specified period in each cycle of a pulsed laser action, and then the laser closes the material for cooling [4]. In recent years, a lot of research has been done on the PLBW of titanium alloy. The microstructure, mechanical properties, and fracture mechanism of welded joints have been discussed. Mohid et al. [5] showed that the pulse energy was the key determinant for welding penetration, while the pulse width highly influenced the weld pool stability and weld bead homogeneity. Junaid et al. [6] used pulsed Nd: YAG laser beam welding and pulsed tungsten inert gas welding to weld 1.6 mm thick Ti-5Al-2.5Sn α titanium alloy sheet. Less residual stresses, deformation and distortion, and superior mechanical properties in PLBW made the process more feasible than pulsed tungsten inert gas welding for Ti-5Al-2.5Sn alloy sheets. Gao et al. [7] studied the effect of weld section and microstructure on mechanical properties of pulsed Nd: YAG laser welded Ti6Al4V alloy under different welding conditions. Kumar et al. [8] conducted experimental and numerical analysis on Nd: YAG laser welded titanium alloy sheet temperature distribution. They found that the elongated grain and regular plate structure in Nd: YAG laser welded joint are the key factors in improving the joint's tensile strength.

For a practical PLBW process of metal sheets assembled in butt joint configuration, the precise control of the assembling clearance has long been a challenge. The existence of machining burrs and assembly errors will lead to forming severe defects, such as misalignment, welding leakage, and penetrating [9]. The research mentioned above on PLBW of titanium alloy shows that PLBW is an exemplary process for titanium alloy welding. However, many studies did not consider the impact of assembling clearance. The existence of assembly clearance increases the complexity of the welding process and affects the morphology of the welding pool and the flow of liquid metal. It is difficult to obtain the temperature distribution of molten pool and keyhole evolution accurately by conventional process experiments. Numerical modeling and simulation can provide insight into the welding process and help to reveal the mechanism of process parameters. In recent years, the numerical simulation of the PLBW process has made significant progress. Satyanarayana et al. [10] built a three-dimensional heat-flow coupling model to simulate heat transfer and Marangoni flow in pulsed Nd: YAG laser welding of Zr–Nb alloy. The calculation of heating and cooling rates facilitated the explanation of microstructure formation in various seam zones. Pang et al. [11] proposed a quantitative model of porosity defects induced by keyhole instability in a titanium alloy's partial penetration CO_2 laser welding. The simulated keyhole depth fluctuations could represent the various trends in pore number and average size for the studied process conditions. Drobniak et al. [12] used multi-physical CFD modeling to study the process of two stainless steel

plates with overlapping configurations. The influence of clearance on fluid dynamics and weld defect appearance was analyzed. Based on the results, adapted beam shapes were proposed that allow for optimized energy distribution and thus an improved weld quality. Hao et al. [13] established a three-dimensional transient numerical analysis model of tungsten inert gas welding with reserved clearance. The model takes into account the loss of total input heat as well as the change in arc pressure produced by the reserved clearance. The modeling findings suggest that increasing the reserved clearance increases the maximum sag of the molten pool.

To sum up, the existence of assembly clearance has a significant impact on the heat transfer and fluid flow in the molten pool. The numerical investigations reported have paid little attention to keyhole and weld pool dynamics modeling and calculation in pulse laser welding of titanium alloys with reserved air gaps. The influence of crucial heat input parameters on heat transfer, keyhole evolution, and fluid flow in the pulse laser tailor-welding process has not been fully solved. Here, we develop a three-dimensional multi-phase and multi-physical field coupling model to simulate the PLBW process of Ti6Al4V titanium alloy plates with reserved air gaps, involving the dynamic behavior of keyholes and molten pools. THINC/LS algorithm and ray tracing algorithm are used to realize free interface tracking and energy calculation on the interface. Using various welding heat input parameters, the transient temperature field, velocity vector, keyhole size, and liquid bridge area were calculated and examined. The effects of welding speed and laser peak power on heat and mass transfer behavior in the PLBW process were investigated.

2. Experimental details

Ti6Al4V alloy plates were used in the experiment, with dimensions of 100 mm × 50 mm × 1.2 mm. Ti6Al4V titanium alloy belongs to the α + β type dual-phase titanium alloy. Its main alloying elements are Al and V, which chemical composition is shown in Table 1. Before welding, the specimens were assembled in a butt way, and a 0.2 mm air gap was reserved. The establishment of the experimental system is shown in Fig. 1.

Table 1 Chemical composition of TC4 titanium alloy (wt%)

Composition	Fe	C	H	O	N	Al	V	Ti
Wt %	0.15	0.03	0.002	0.08	0.01	6.0	4.0	Bal.

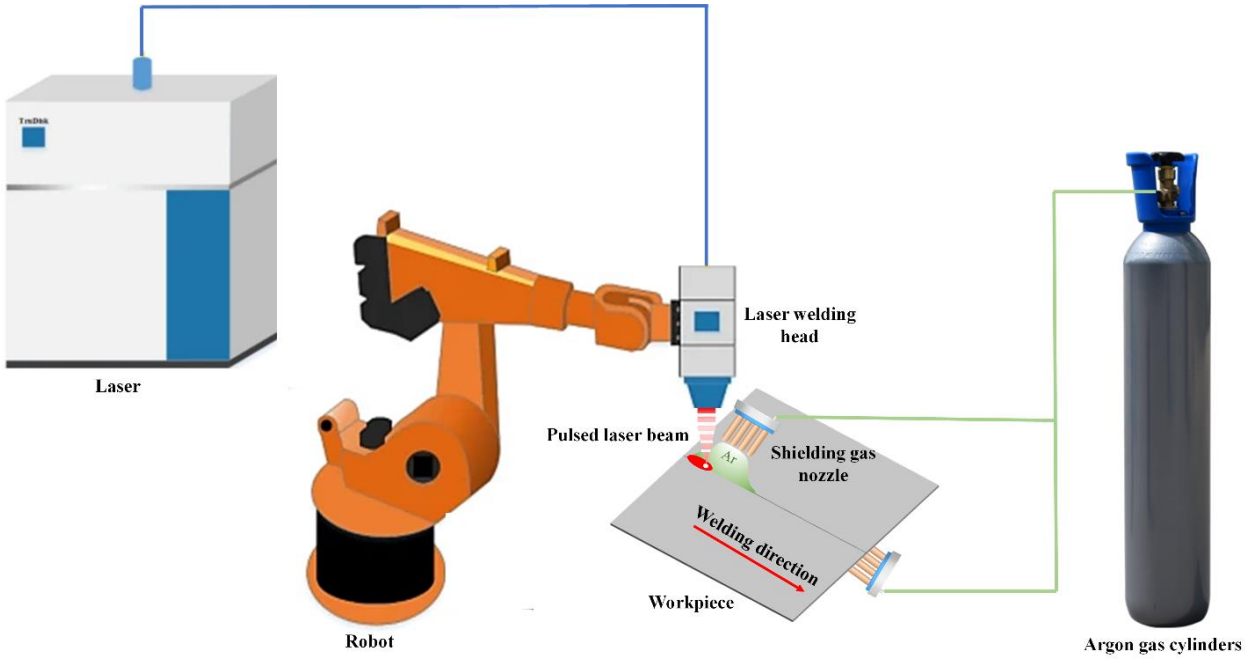

Fig. 1. Experimental system setup for the PLBW of Ti6Al4V alloy plate with reserved clearance.

The welding equipment is a Trumpf Trudisc 4001 disc laser with a wavelength of 1.03 μm, a maximum laser power of 4 kW. The laser waveform is modulated as shown in Fig. 2, and the spot diameter is 0.7 mm. Pure argon was supplied to the top and bottom surfaces of the sample, with a protective gas flow of 30 L/min on the top surface and 15 L/min on the bottom surface.

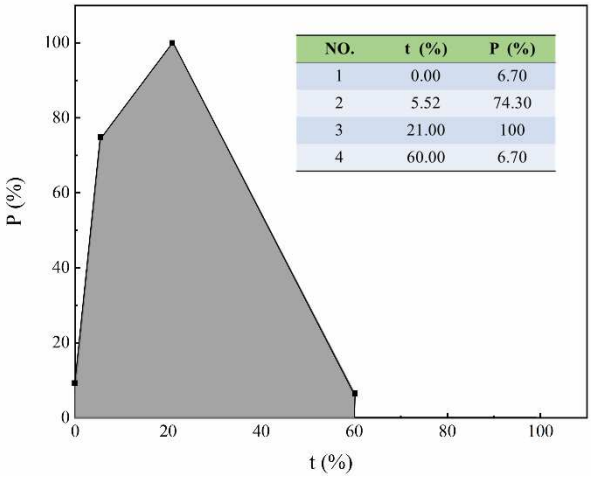

NO.	t (%)	P (%)
1	0.00	6.70
2	5.52	74.30
3	21.00	100
4	60.00	6.70

Fig. 2. The pulse shape of the laser.

Welding process parameters are shown in

Table 2. The influence of different heat input conditions on the dynamic behavior of the keyhole and weld pool was studied by changing the welding speed and peak power. After welding, metallographic samples are prepared according to standard procedures. The weld cross-section was obtained by wire cutting the middle of the specimen and then ground and polished to 1 μm diamond paste. The metallographic sample of the weld

section was etched with Kroll solution (2% HF+ 10% HNO_3 + 88% H_2O) and observed by a 4XC metallographic microscope.

Table 2 Critical process parameters of PLBW

Case No.	Peak laser power (W)	Welding speed (m/min)	Pulse frequency (HZ)	Air gap size (mm)	Shielding gas flow rate at top (L/min)	Shielding gas flow rate at root (L/min)
1	2000	1.8	40	0.2	30	15
2	2200	1.8	40	0.2	30	15
3	2400	1.8	40	0.2	30	15
4	2400	1.6	40	0.2	30	15
5	2400	2.0	40	0.2	30	15

3. Mathematical modeling

3.1 Modeling simplification

The critical physical factors in the PLBW process of thin plate with reserved clearance are not only basic convection in the molten pool to transfer heat but also critical physical processes that affect the molten pool and keyhole change, such as multiple beam reflections, Rayleigh scattering, Fresnel absorption, and solid-liquid-gas phase transitions. To ensure accuracy and improve the calculation efficiency, the following assumptions are made:

1. The computational domain consists of incompressible, Newtonian, and laminar fluids.
2. The original laser beam consists of a limited number of sub-beams, which irradiate vertically on the surface of the workpiece.
3. The reflection of the sub-beam at the liquid-gas interface follows the principle of specular reflection.
4. Due to the weak ionization plume effect, the inverse bremsstrahlung absorption can be neglected [14].
5. In view of the weak ionization of metal vapor in laser welding, the mixture of metal vapor and shielding gas argon is simplified to a single argon phase [15].
6. An additional surface heat source is used to equivalent the plume heating effect around the keyhole opening.

3.2 Governing equations

For incompressible fluids, the mass conservation is [16]:

$$\nabla \cdot \vec{u} = 0 \tag{1}$$

where $\vec{u}$ is the velocity field of fluid.

The momentum equation considers the momentum source terms, including gravity, heat buoyancy, Darcy resistance in solidification and melting regions, and recoil pressure [17].

$$\frac{\partial}{\partial t}(\rho \vec{u}) + \rho(\vec{u} \cdot \nabla)\vec{u} = -\nabla p + \eta \nabla \cdot \left[\nabla \vec{u} + (\nabla \vec{u})^T\right] + \vec{S}_m \tag{2}$$

$$\vec{S}_m = f_g + f_b + f_d + f_r \tag{3}$$

Here, t, ρ, p, η, f_g, f_b, f_d and f_r denote time, mass density, pressure, dynamic viscosity, gravity, heat buoyancy, Darcy resistance, and recoil pressure, respectively.

$$f_g = -\rho \vec{g} \tag{4}$$

$$f_b = -\rho \vec{g} \beta (T - T_l) \tag{5}$$

$$f_d = -K_0 \frac{(1-\alpha_l)}{\alpha_l^3 + c}(\vec{u} - \vec{u}_0) \tag{6}$$

$$f_r = \frac{AB_0}{\sqrt{T}} \exp\left(\frac{-M_a H_v}{N_a k_b T}\right) \cdot \vec{n} \cdot \delta(\varphi) \tag{7}$$

In Eq. (5), β, T_l are thermal expansion coefficient and liquidus temperature. In Eq. (6), α_l is liquid volume fraction, c is usually 10^{-3} to 10^{-5}. K_0 is Darcy constant related to the volume fraction of the liquid phase which in this paper is valued at 2×10^7. In Eq. (6), A and B_0 denote pressure constant and evaporation constant. M_a, L_v, N_a, k_b, $\vec{n}$ are molar mass, evaporation latent heat, Avogadro constant, Boltzmann constant and surface normal vector respectively.

To improve the numerical calculation speed, the liquid fraction α_l changes linearly with temperature:

$$\alpha_l = \begin{cases} 1 & (T > T_l) \\ \dfrac{T - T_s}{T_l - T_s} & (T_s < T < T_l) \\ 0 & (T_0 < T < T_s) \end{cases} \tag{8}$$

with T_s being solidus temperature and T_0 being reference temperature.

Considering the energy balance of laser heat flow, the pulse laser welding process of the thin plate should follow the energy conservation equation [18]:

$$\frac{\partial}{\partial t}(\rho h) + \nabla \cdot (\rho h u) = \nabla \cdot (k \nabla T) + S_Q \tag{9}$$

Here, h is enthalpy and k is heat conductivity. S_Q is the energy source term consists of Rayleigh scattering Q_{Rs} and Fresnel absorption Q_{Fa} generated during the continuous laser output.

3.3 Free surface tracking algorithm

The volume of fluid (VOF) [19] and level set method (LS) [20] have been widely used to solve the two-phase flow problem. In this paper, the THINC/LS algorithm reported by Qian et al. [22] is used to solve the keyhole evolution under laser-induced evaporation and oscillation. The calculation accuracy of interface

geometric features can be considerably improved with this method, which combines the THINC and LS functions. In a vector space, the Level Set approach defines a symbolic distance function. The Level Set function has the following attributes:

$$\phi(x,t)=\begin{cases} dist(x,\partial V) & X\in V^1 \\ 0 & X\in \partial V \\ -dist(x,\partial V) & X\in V^2 \end{cases} \tag{10}$$

The THINC function uses the hyperbolic tangent function to fit the interface discontinuity solution within the range of [0,1]. When its value is 0.5, it represents the moving interface, which reads

$$H(x,t)=\frac{1}{2}\left(1+\tanh\left(\beta\phi(x,t)\right)\right) \tag{11}$$

Here, β is a parameter used to control the thickness of the interface. The Heaviside step function can be approximated by increasing the value of β. The average value of the THINC function $\bar{H}$ represents the volume fraction of the fluid specified in the VOF method.

$$\bar{H}(t)=\frac{1}{|\Omega|}\int_{\Omega} H(x,t)dxdydz \tag{12}$$

where Ω denotes the computing domain.

The evolution of the keyhole surface can be described by interface moving functions:

$$\begin{aligned} &\frac{\partial\phi}{\partial t}+u\cdot\nabla\phi=0 \\ &\frac{\partial H}{\partial t}+\nabla\cdot(uH)=0 \end{aligned} \tag{13}$$

According to Eq. (10) and Eq. (11), when $\phi(x,t)=0$ or $H(x,t)=0.5$ indicates the moving interface. THINC / LS method can update the LS function and THINC function at the same time to achieve high-order interface representation and numerical conservatism.

3.4 Heat source model

In the PLBW process, the ray-tracing algorithm was created for heat source modeling. Beam discretization, beam-interface intersection, multi-reflections, Rayleigh scattering, and Fresnel absorption are all part of the ray-tracing process [23]. The laser spot is discretized into a finite number of beams using a two-dimensional uniform grid, and the laser power density distribution is ideally Gaussian. The incident sub-beam advances gradually along the unit vector, and the energy attenuation caused by Rayleigh scattering Q_{Rs} can be calculated along the laser propagation path. When the free interface meets the laser beam, the Fresnel absorption Q_{Fa} can be calculated.

$$Q_{Rs}=\sum_{n=1}^{bn}\sum_{m=1}^{mr}q_{m-1,n}\left(1-\exp\left(\int_{m-1}^{m}k_r dl\right)\right) \tag{14}$$

$$Q_{Fa}=\sum_{n=1}^{bn}\sum_{m=1}^{mr}q_{m-1,n}\exp\left(-\int_{t-1}^{t}\alpha_{Rs}dl\right)\left(\vec{I}_t\cdot\vec{n}_t\right)\cdot\alpha_{Fa}\left(\theta_t\right) \tag{15}$$

Here, l, k_r, m, mr, n, bn are the beam propagation distance after divergence, Rayleigh scattering coefficient, multi-reflection times, total number of multiple reflections, sub-beam number, and total number of sub-beams, respectively. $\vec{I}$, $\vec{n}_t$ are unit incident vector and unit normal vector. α_{Rs}, α_{Fa} are the coefficients related to Rayleigh scattering attenuation and Fresnel absorption respectively. α_{Rs} and α_{Fa} is calculated as follows:

$$\alpha_{Rs}=\left(\frac{8}{3}\left(\frac{2\pi r_p}{\lambda}\right)^4\left|\frac{m^2-1}{m^2+1}\right|^2-\frac{8\pi r_p}{\lambda}\mathrm{Im}\left\{\frac{m^2-1}{m^2+1}\right\}\right)\pi r^2 N \tag{16}$$

$$\alpha_{Fa}\left(\theta\right)=1-\frac{1}{2}\left(\frac{1+\left(1-\varepsilon\cos\theta\right)^2}{1+\left(1+\varepsilon\cos\theta\right)^2}+\frac{\varepsilon-2\varepsilon\cos\theta+2\cos^2\theta}{2\varepsilon+2\varepsilon\cos\theta+2\cos^2\theta}\right) \tag{17}$$

In Eq. (16), r_p, λ, m, N denote vapor particle radius, laser wavelength, complex refractive index and particle density respectively. In Eq. (17), θ is the reflection angle of the sub-beam. According to the Hagen-Rubens relationship, α_{Fa} is highly dependent on the reflection angle.

Under the action of laser irradiation, the metal melts and evaporates to form a keyhole, forming a high-energy plasma above the molten pool. The lack of plume heating in the modeling will lead to the mismatch between the simulated molten pool width and the experimental molten pool width. As suggested by Yang et al [24], two additional surface heat sources are applied on the top and bottom surfaces of the workpiece to equivalent plume heating effect. And the heat flux satisfies the following equation:

$$Q_P=\frac{3k_0P_L\left(t\right)}{\pi r_1^2}\exp\left(\frac{-3r^2}{r_1^2}\right)\cdot\xi_1+\frac{3k_0P_L\left(t\right)}{\pi r_2^2}\exp\left(\frac{-3r^2}{r_2^2}\right)\cdot\xi_2 \tag{18}$$

Here, k_0, P_L, t are heat source efficiency, laser power, and time. With r_1, r_2 representing the heat source radius of surfaces and ξ_1, ξ_2 representing the absorption coefficients.

3.5 Computational domain, boundary condition, and material parameter

As shown in Fig. 3, a computation domain of 5 mm × 2.2 mm × 1.5 mm is established and the mesh model consists of 132,000 cube elements with a grid step of 0.05 mm. The domain is initialized to the liquid phase

region and the gas phase region. The initial liquid phase zone is filled with Ti6Al4V titanium alloy and separated by a reserved air gap of 0.2 mm. The thermos-physical properties of Ti6Al4V alloy are shown in Table 3 [25]. The top and bottom boundaries of the domain are set to pressure outlet and adiabatic. The boundary conditions of the walls in terms of energy are convective heat transfer and thermal radiation [26], which reads:

$$-k\frac{\partial T}{\partial n}=h_c\left(T-T_0\right)+\varepsilon\sigma\left(T^4-T_0^4\right) \tag{19}$$

Here, ε, h_c, σ, T_0 are surface emissivity, Stefan-Boltzmann constant, convective heat transfer coefficient and reference temperature.

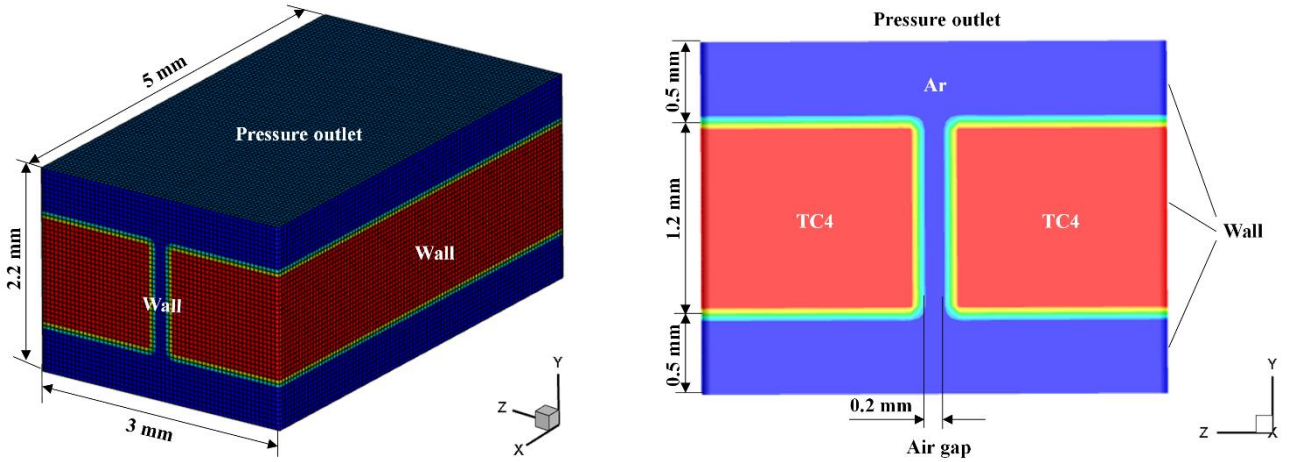

Fig. 3. The dimensions and boundary conditions of the calculation domain.

3.6 Simulation implementation

The welding process parameters applied in the simulation, such as laser spot diameter, laser peak power, welding speed, and other related parameters are highly consistent with the experimental parameters. The numerical model including calculation domain, three-dimensional mesh, and Ti6Al4V thermos-physical property parameters was loaded into fluent 19.0. The momentum and energy source terms are coded into a user-defined function (UDF) in C language. The pressure implicit algorithm is used to solve the governing equations, which are discretized using the finite volume approach. The PLBW process was simulated for 100 ms with a physical time step of 0.001 ms.

Table 3 Thermophysical properties of Ti6Al4V alloy for numerical calculation

Physical parameters	Symbol	Unit	Value
Density	ρ	$kg \cdot m^{-3}$	4420
Solidus temperature	T_s	K	1878
Liquids temperature	T_l	K	1923
Evaporation temperature	T_v	K	2740
Thermal expansion coefficient	β		1.1×10^{-5}
Specific heat (T_l)	C_P	$J \cdot kg^{-1} \cdot K^{-1}$	546759
Heat conductivity (T_l)	λ	$W \cdot m^{-1} \cdot K^{-1}$	28.4
Latent heat of fusion	L_m	J	2.86×10^{5}
Latent heat of evaporation	L_v	J	4.19×10^{6}
Dynamic viscosity (T_l)	η	$Kg \cdot m^{-1} \cdot s^{-1}$	3.25×10^{-3}
Surface tension coefficient	σ	$N \cdot m^{-1}$	1.577

4. Results and discussions

4.1 Verification of simulation results with weld cross-section

As shown in Fig. 4, well-formed and defect-free weld beams composed of continuously overlapping weld spots can be obtained by using different welding speeds and laser peak power. Fig. 5 shows the simulated weld pool morphology compared with the experimentally determined weld cross-section. The characteristic dimensions are measured and listed in Table 4. The calculated surface width (SW), half-penetration width (HW), and root width (RW) are 0.50-7.39% smaller than the experimental results. The primary cause of this error is that the secondary heating effect of the metal vapor plume around the keyhole opening is not taken into account.

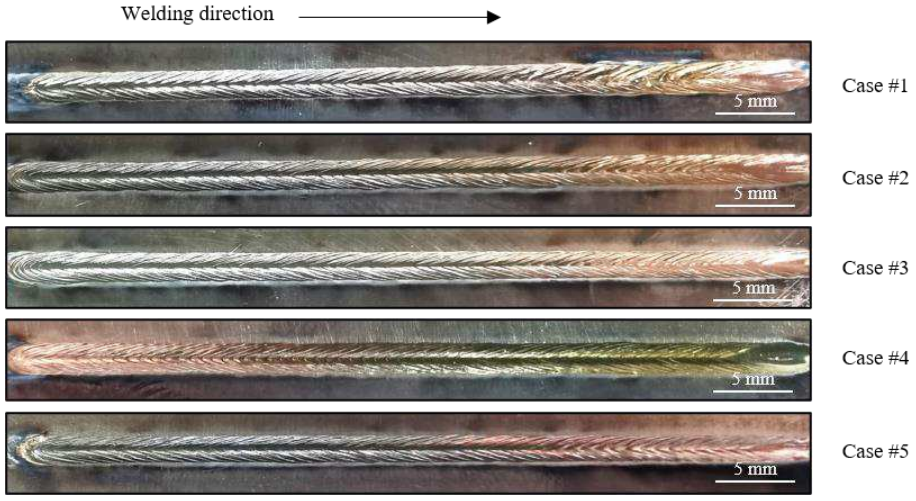

Fig. 4. Surface formation of pulsed laser-welded Ti6Al4V specimen in varying cases.

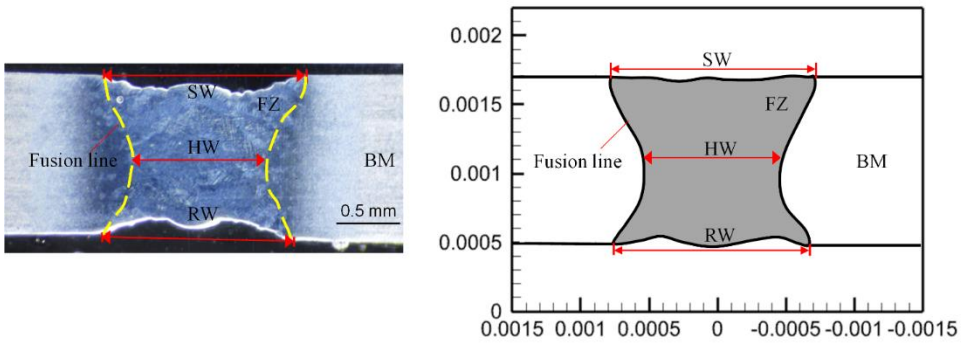

Fig. 5. The simulated weld dimensions in comparison to experimental results.

Table 4 The dimensional deviation between numerical simulations and experimental results

Dimensions		Case No.				
		1	2	3	4	5
Peak laser power (kW)		2.0	2.2	2.4	2.4	2.4
Welding speed (m/min)		1.8	1.8	1.8	1.6	2.0
surface width (mm)	Experimental	1.44	1.46	1.48	1.61	1.45
	Simulated	1.51	1.47	1.52	1.54	1.46
	Deviation(%)	4.86%	0.68%	2.70%	4.35%	0.69%
Half-penetration width (mm)	Experimental	0.88	1.00	0.99	1.00	0.97
	Simulated	0.95	0.99	1.06	0.99	1.00
	Deviation(%)	7.95%	1.00%	7.07%	1.00%	3.09%
Rood width (mm)	Experimental	1.23	1.26	1.35	1.39	1.33
	Simulated	1.32	1.21	1.39	1.48	1.38
	Deviation(%)	7.32%	3.97%	2.96	6.47%	3.76%

4.2 Evolution characteristics of temperature field, velocity field and liquid bridge profile

Using case 3 as an example, Fig. 6 depicts the evolution of the molten pool temperature field and phase interface in the first laser pulse period. The workpiece is colored by the temperature legend of 400 ~ 2600 K, and the solidus of the molten pool is drawn by the black line. At the beginning of the PLBW, the edge of the thin plate with a gap is heated to the evaporation temperature as the laser power is increasing. With the irradiation of the laser at t = 0.5 ms, two pits emerge on the edge of the sheet, but the two sheets are still separated at this moment. With more melting and penetration of the keyhole, the molten metal accumulated rapidly in the next 1ms, and a liquid bridge was established in the gap. In the period of 2 ms to 5 ms, the width and length of the molten pool increase with the increase of laser power. Looking in the - Y direction, the opening at the bottom of the keyhole becomes larger, reflecting the slight changes in the shape of the keyhole. When the laser power reaches the maximum, the opening at the top of the keyhole is significantly larger than before, and the length and width of the top molten pool also reach their maximum. After t = 5 ms, the laser power is in the decline stage. With the decrease in temperature, the falling recoil pressure can not balance the surface tension and

hydrostatic pressure, resulting in the rebound of the keyhole surface from bottom to top and the backfilling of molten metal, which is consistent with the research reported by Chen et al. [18]. When the laser power drops to zero at t = 15 ms, the keyhole at the bottom is closed and disappears rapidly within microseconds. During the cooling process, the liquid bridge is further solidified into metal in the air gap, and the size of the molten pool is significantly reduced.

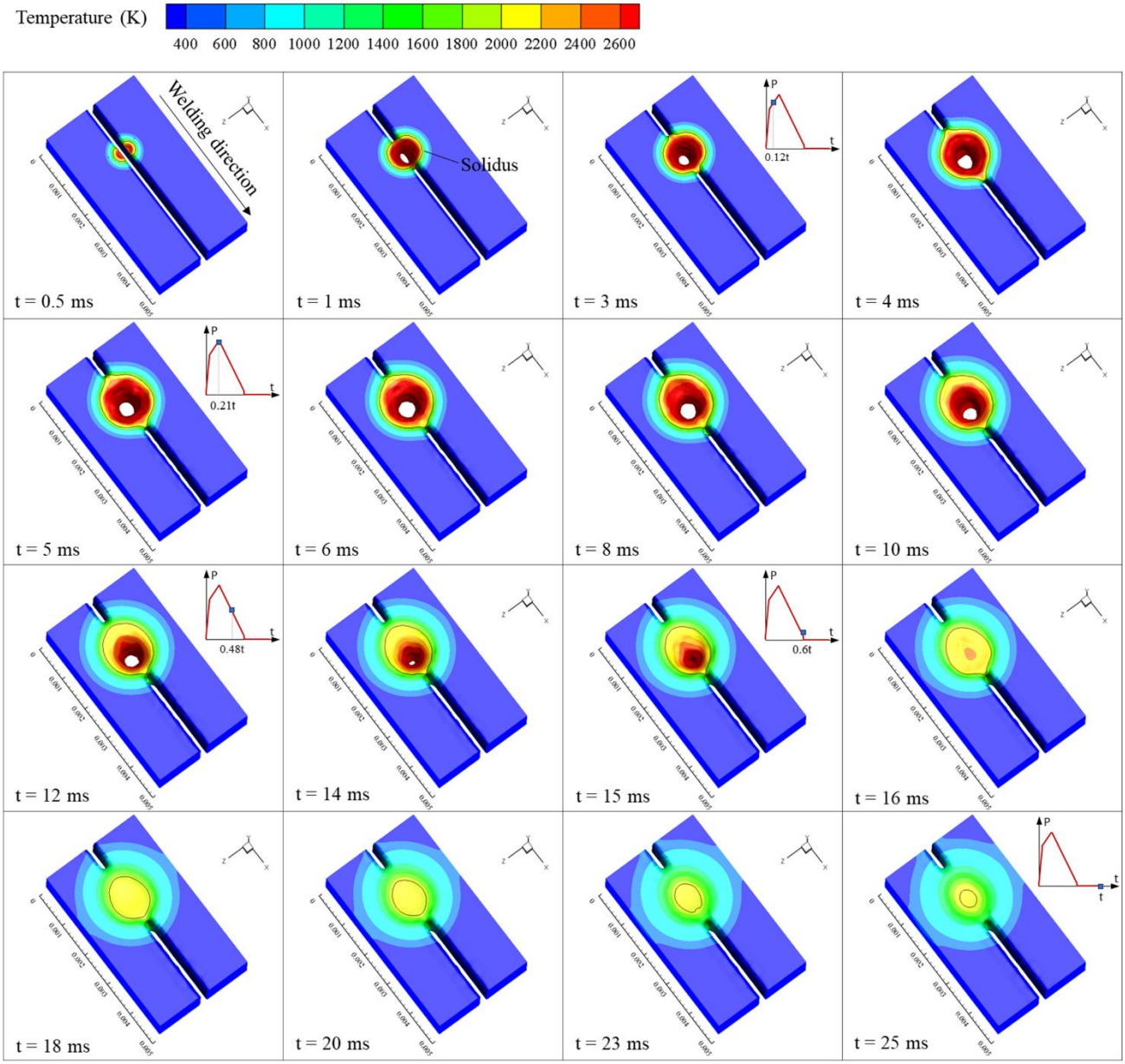

Fig. 6. Evolution of temperature field and phase interface of Case 3 in the first pulse period.

The second laser pulse period has a calculation range of 25 ms to 50 ms. When the laser beam is re-irradiated from 25 ms to 26 ms, a portion of the solidified metal from the first pulse cycle is remelted and recoiled downward to form the back of the keyhole, as shown in Fig. 7. The molten metal forms a new liquid bridge on the front of the keyhole in the next microsecond. The length and diameter of the molten pool greatly

grow over the 27-30 ms period, which is identical to the calculated results of the first pulse period. The top surface of the molten pool, on the other hand, resembles a droplet, which is a unique phenomenon of the second pulse period when compared to the first pulse period. During the remaining time, the dynamic behaviors of the molten pool such as temperature drop, keyhole rebound, volume shrinkage, and cooling occur due to the decrease in laser power. The keyhole oscillation and rebound lasted from 31 ms to 41 ms. At t = 40 ms, the keyhole is closed at the bottom. The keyhole rebound process not only causes the liquid bridges around the keyhole to merge but also makes the second welding joint partially overlap with the first welding joint. This overlap increases the length of the connection between the two welding joints.

When the pulsed laser beam is used to weld Ti6Al4V thin plate with a gap, the velocity field of the molten pool has the characteristics of metal vapor eruption and molten metal convection. The shift in velocity field around the keyhole is depicted in Fig. 8. The eruption speed of metal vapor is much higher than that of molten metal flow. The maximum eruption speed of metal vapor can reach 90.54 m/s, while the flow rate of liquid metal is lower than 2.0m/s, which is consistent with the research results of Chang [27] et al. The color arrow is used to show the flow velocity of molten metal due to the considerable difference between gas and liquid phase velocity. The arrow points in the same direction as the flow, and different colors represent varying flow velocities. The magnitude of the gas phase velocity is indicated by the length of the black arrow. The velocity vector of molten metal is perpendicular to the keyhole surface during laser heating and keyhole growth, as observed at 1.5 ms. The metal vapor eruption outside the keyhole becomes more powerful as the laser power increases. When t = 5.5 ms, the laser power reaches its maximum and then progressively falls, the metal vapor eruption weakens, and Marangoni convection is observed in the molten pool. The velocity of molten metal near the keyhole is larger than that at the molten pool's edge due to the temperature gradient. Under the operation of Marangoni shear stress, it can be observed that molten metal flows from the high-temperature keyhole area to the low-temperature area of the molten pool at t = 10 ms. The rebound pressure drops to zero during the keyhole contraction stage, and the molten metal flows to the keyhole wall. Under the operation of large surface tension at the bottom of the keyhole, a certain amount of inward flow compensates for the rebound of the keyhole in the bottom area of the molten pool. When the keyhole spring back is complete, the fluid has a steady bottom-up flow.

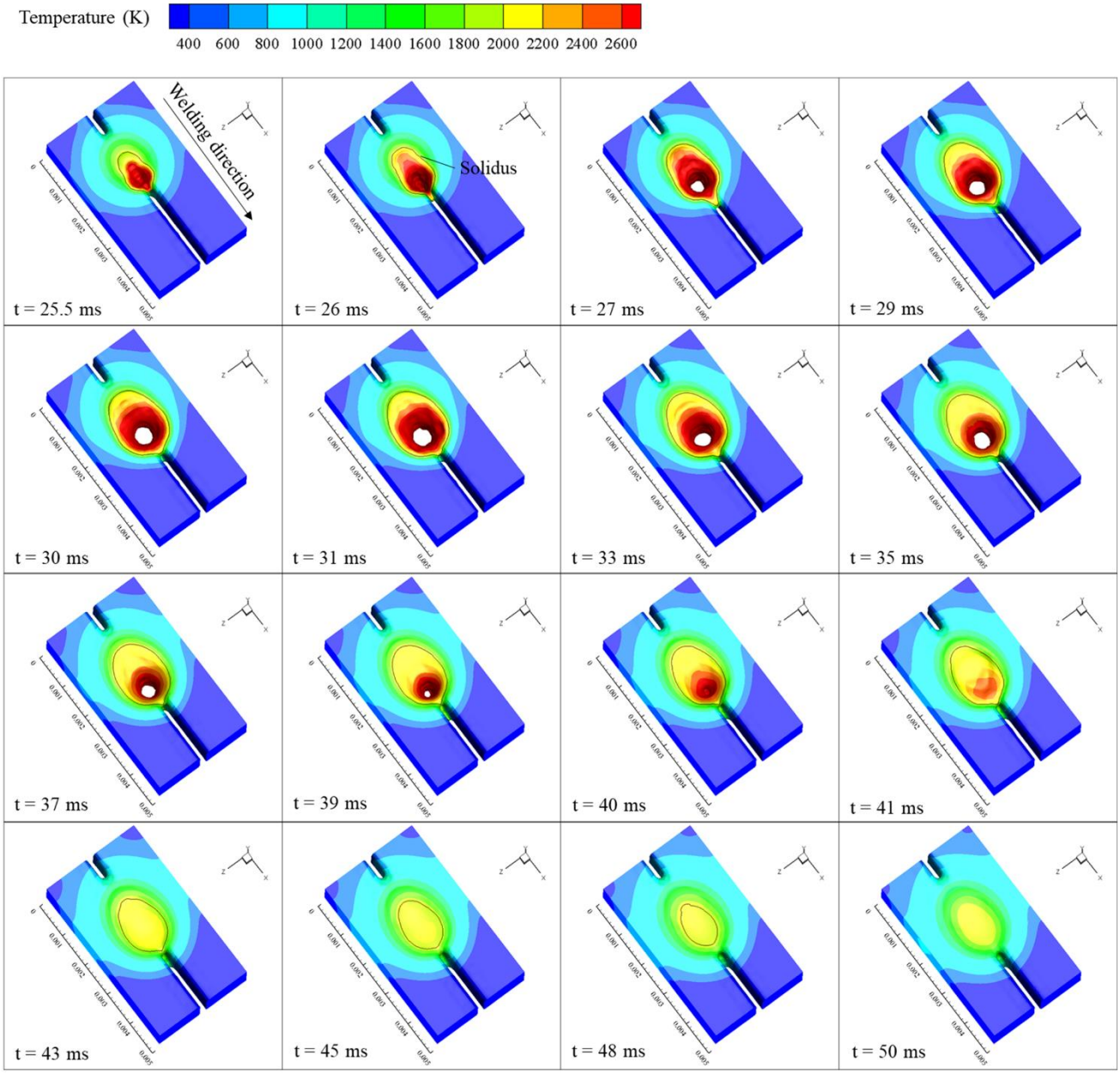

Fig. 7. Evolution of temperature field and phase interface of Case 3 in the second pulse period.

To further describe the Ti6Al4V thin plate connection process on the air gap, the regions with liquid volume fraction greater than 0.5 in the X-Y plane of z = 0 were extracted. The appearance of molten metal indicates that the thin plate has a connection on the gap, as presented at 1.5 ms in Fig. 9. The first liquid bridge is located in the middle of the thin plate's thickness direction, rather than on its upper and lower surfaces. The liquid bridge formed on the gap gradually expands as the welding time increases. The keyhole divides the liquid bridge into the front and rear parts, and there is no liquid bridge inside the keyhole. Under the influence of gravity, the molten metal travels downhill, causing visible liquid sag at the root surface of the workpiece. At the moment of 15 ms, the laser power drops to zero and the recoil pressure rapidly drops to zero. The keyhole shrinks from

bottom to top as surface tension increases, allowing the liquid bridge to be fused. The molten metal shrinks and cools after one pulse period, creating two noticeable pits on the upper and lower sides of the thin plate, which is quite different from the relatively flat weld obtained by PLBW without gap [7]. When the laser heat source is turned back on at 25.5 ms, the top of the liquid bridge substantially alters. The liquid bridge is separated again with the appearance of the keyhole, and a huge amount of liquid metal accumulates at the root surface of the workpiece. The liquid bridge created in the second pulse period displays evident expansion in the welding direction as compared to the first pulse period.

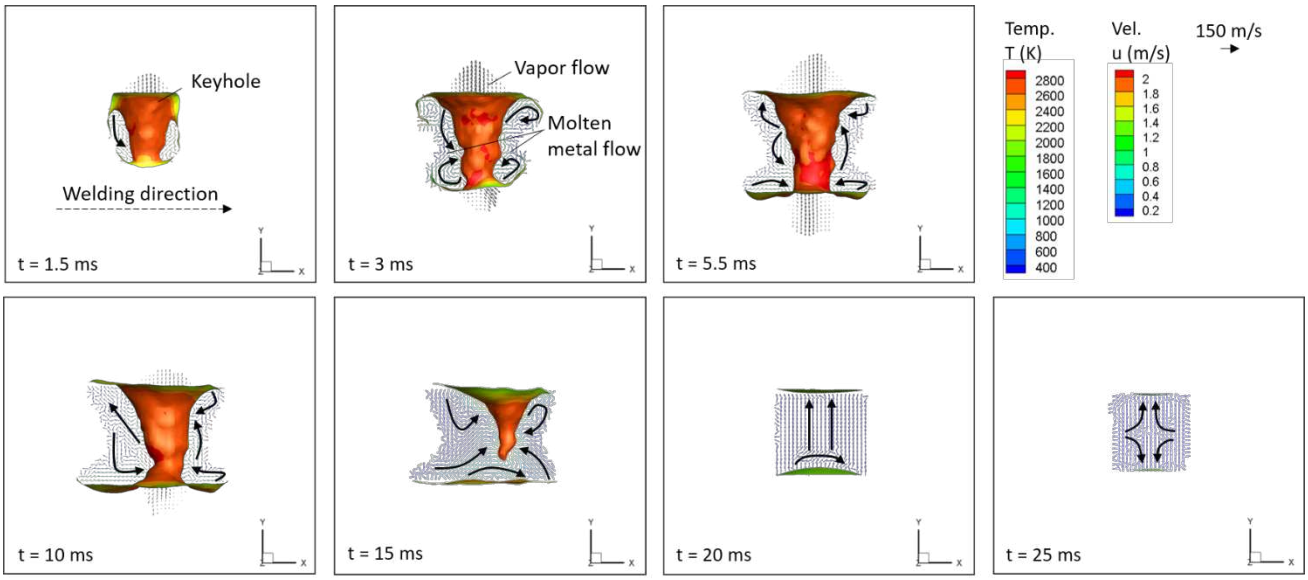

Fig. 8. Keyhole and transient velocity field in the X-Y plane of z = 0.

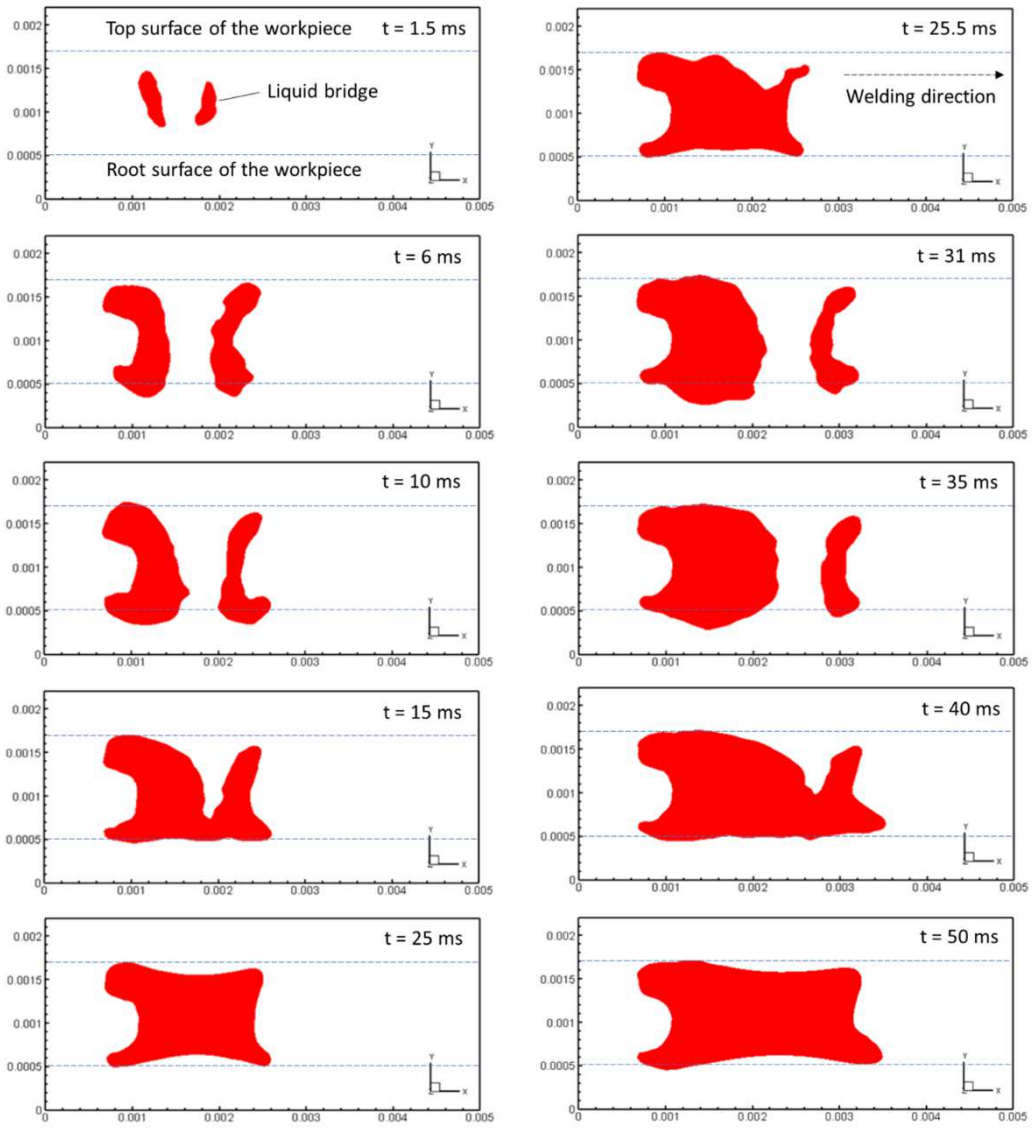

Fig. 9. The shape of the liquid bridge at different times in the X-Y plane of z = 0.

4.3 Effects of welding speed and peak laser power on keyhole and weld pool dynamics

The created model was used to simulate PLBW under varying peak power and welding speed to investigate the influence of heat input on the dynamic behavior of the molten pool. Fig. 10 depicts the keyhole and temperature field properties under various heat input circumstances. The dynamic evolution process of a molten pool mimicked by diverse situations is comparable. The keyhole is always in three stages including that keyhole emerges first, then gradually creates a through-hole, the through-hole retains the oscillation condition, and ultimately the keyhole shrinks and vanishes when the laser power is reduced to zero. As presented at 2 ms in Fig. 10, when the laser peak power is increased from 2000 W to 2400 W, the keyhole creation speed is accelerated, but the increase in welding speed has no significant influence. The keyhole profile becomes more curved as the laser peak power rises as shown at 10 ms, suggesting that the vibration of the keyhole wall is enhanced. The temperature field of the molten pool extends and the temperature of the keyhole wall rises as the

laser peak power rises and the welding speed falls. As the welding heat input increases, the volume shrinkage of the molten pool becomes more visible due to the rise in the cooling time, as exhibited at 20 ms.

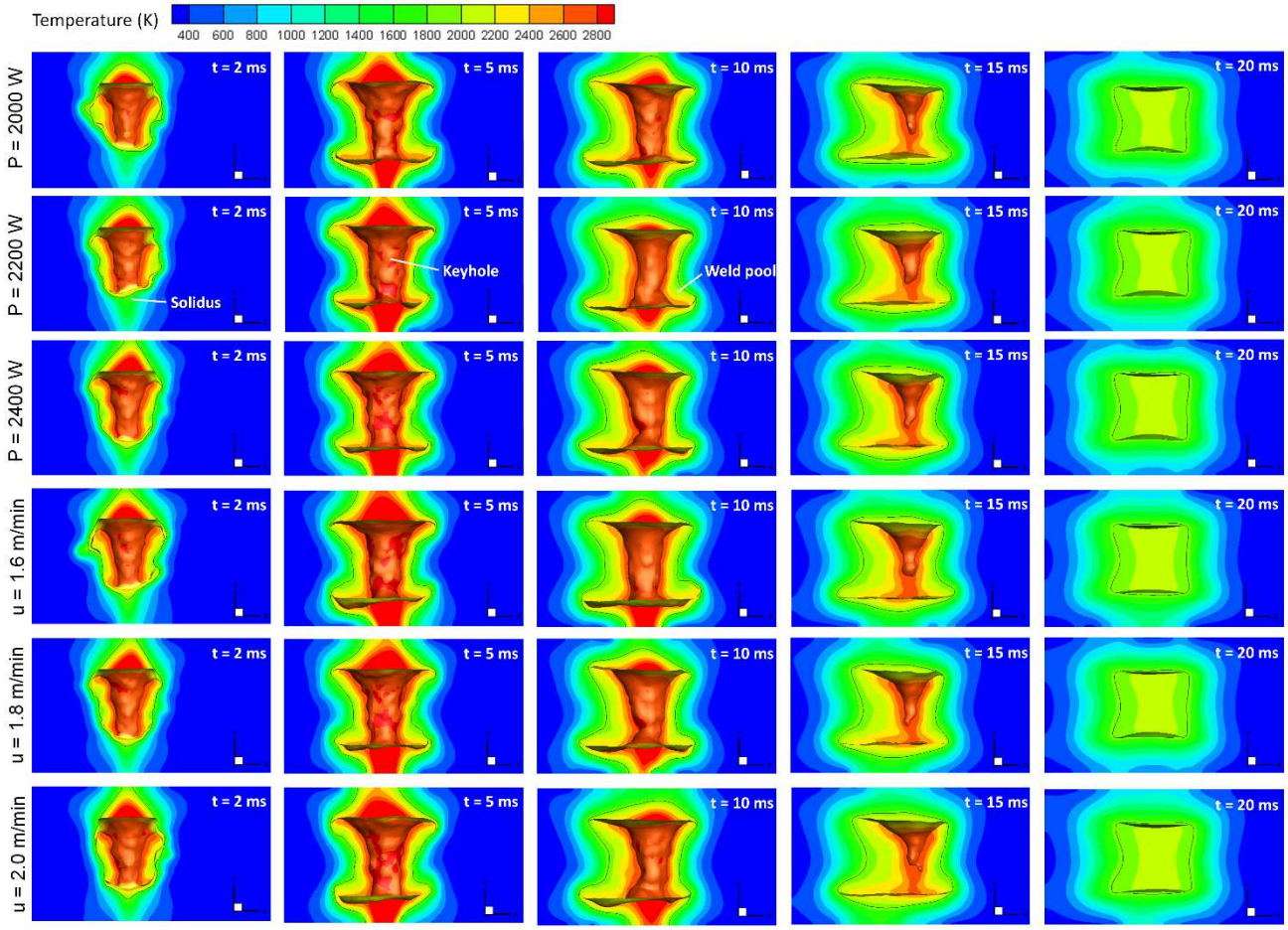

Fig. 10. Characteristics of the keyhole and temperature field under different peak laser power and welding speed.

For further research, Fig. 11 depicts the change in keyhole depth across two pulse cycles with varying peak power. The keyhole depth varies regularly, keeping up with the three stages of keyhole evolution. The depth of the keyhole progressively grows, the maximum depth of the keyhole can reach 1.175 mm, then it remains horizontal, and ultimately it gradually declines to zero. The vibration of the keyhole happens from time to time during the stage of keeping the depth of the keyhole horizontally. Using a peak power of 2000 W as an example, as the laser beam's propagation distance rises, the energy attenuation produced by Rayleigh scattering becomes more apparent, resulting in a fall in the recoil pressure at the bottom of the keyhole. At t = 13.96 ms, the keyhole vibrates fiercely, the depth of the keyhole drops to 0.875 mm, rebounds to 1.175 mm, then shrinks again at 15 ms, and disappears in the next microsecond. Comparing the keyhole depth under different peak power, it is discovered that the keyhole exists for the longest duration in the second cycle when the laser peak power is 2200 W.

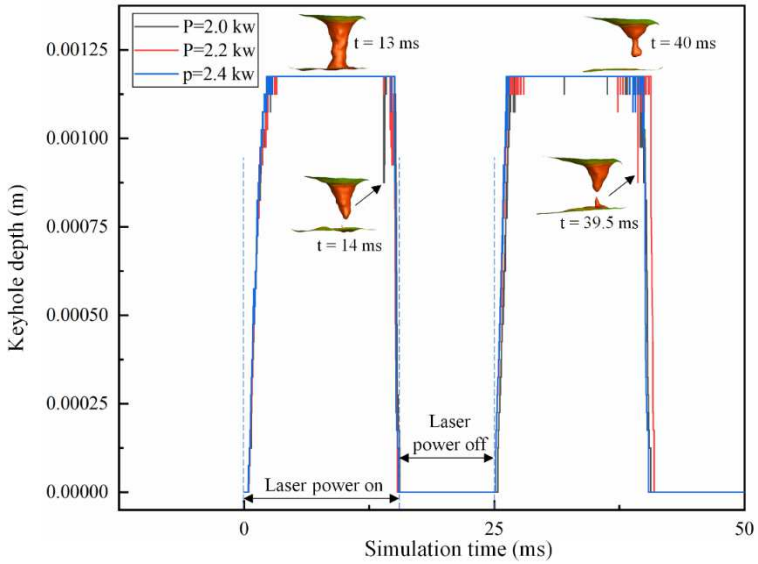

Fig. 11. Keyhole depth changes in two pulse periods under different peak laser power.

4.4 Effects of welding speed and peak laser power on liquid bridge profiles

Fig. 12 shows the evolution of the liquid bridge profile in a pulse cycle under different peak laser power conditions. The increased peak laser power makes it simple to build more liquid bridges on the gap at 1.5 ms when the laser is starting to melt the thin plate. With the increase of welding time, under the action of gravity, the liquid bridge under different peak laser power shows different sagging. At 15 ms, the keyhole shrinks from bottom to top, and the separated liquid bridge generates a connection. When the peak laser power is varied, the liquid bridge profile changes somewhat. When the peak power is high, some of the liquid bridge is below the lower surface of the workpiece, and when it is low, the liquid bridge shrinks above the lower surface. This is because a higher peak power results in a larger welding heat input, longer cooling, and shrinkage times for molten metal. The liquid bridge under various peak laser power finished contracting at 25 ms. Fig. 13 shows the evolution of liquid bridge morphology in a pulse cycle under different welding speeds. Comparing the liquid bridge profile under different welding speeds, it can be found that there is no obvious difference in the liquid bridge profile at 1.5 ms, indicating that in the initial state of welding, the influence of welding speed changes on sheet melting is not obvious. When the welding speed increases, the heat input decreases, the melting amount of the sheet decreases, and the sagging phenomenon of the liquid bridge is improved, as shown in 5.5 ms.

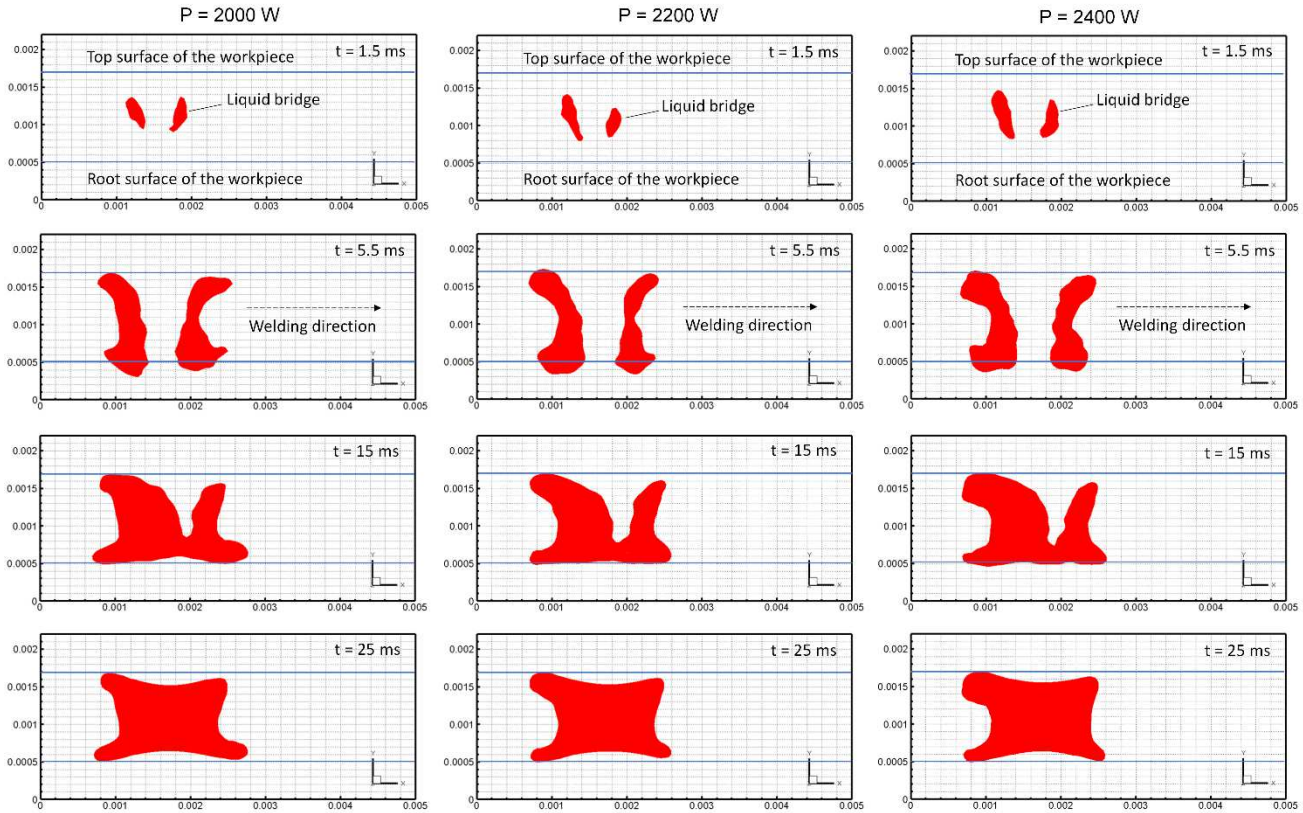

Fig. 12. Characteristics of liquid bridge profile along the welding direction under different peak laser power.

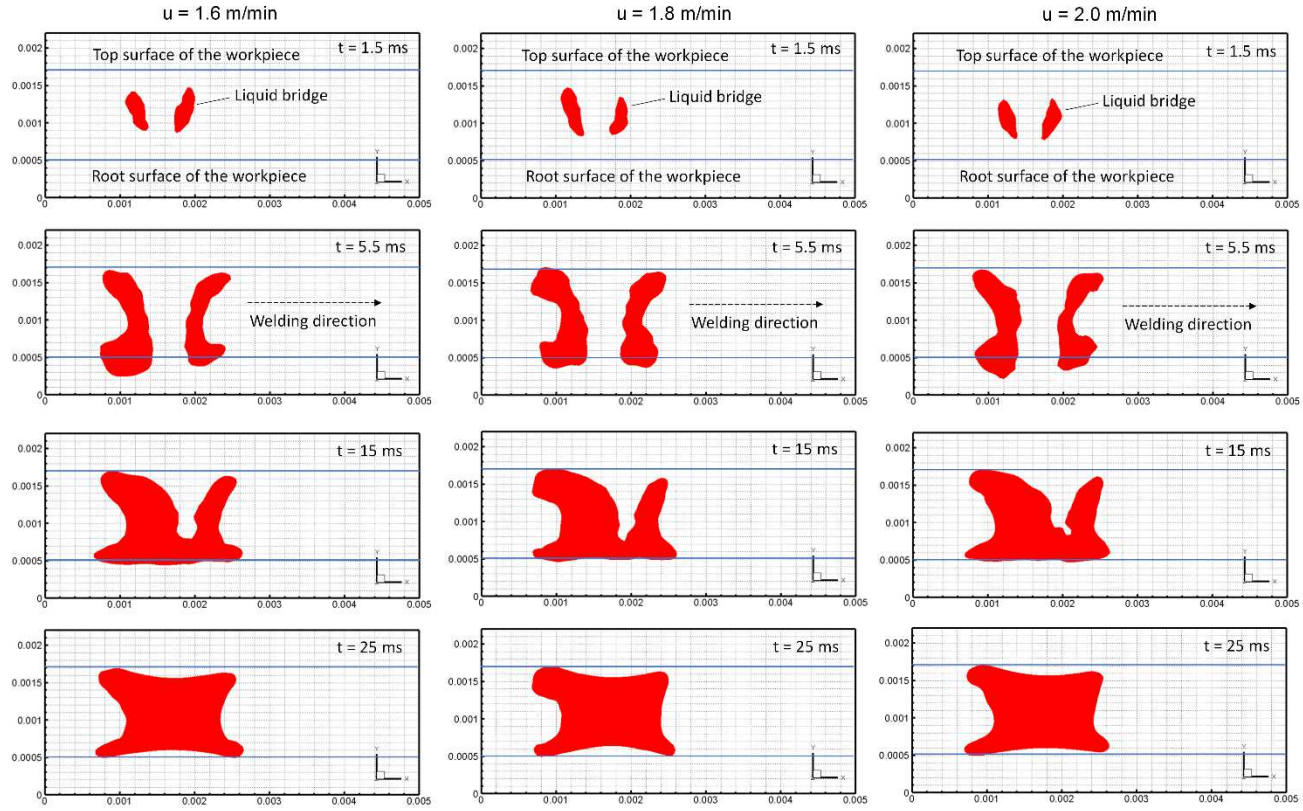

Fig. 13. Characteristics of liquid bridge profile along the welding direction under different welding speeds.

To further explore the influence of heat input conditions on the liquid bridge profile at the z = 0 plane, the liquid bridge area at different times in two pulse cycles was measured, as shown in Fig. 14. By observing Fig.

14 (a), it can be found that the peak laser power has a great influence on the liquid bridge area in the initial state, as previously discussed. With the increase of peak laser power, the liquid bridge area at different welding times increases synchronously. Under different peak laser power, the change of liquid bridge area with welding time tends to be consistent. Compared with the peak laser power, the welding speed has no significant effect on the liquid bridge area in the first pulse cycle, as shown in Fig. 14 (b). The area of the liquid bridge formed at different welding times grows in the second pulse period as the welding speed increases. And when the welding speed increases, the liquid bridge area expands more frequently, indicating that the welding speed increases and the molten pool's stability improve, which is consistent with the conclusion of Chen [28].

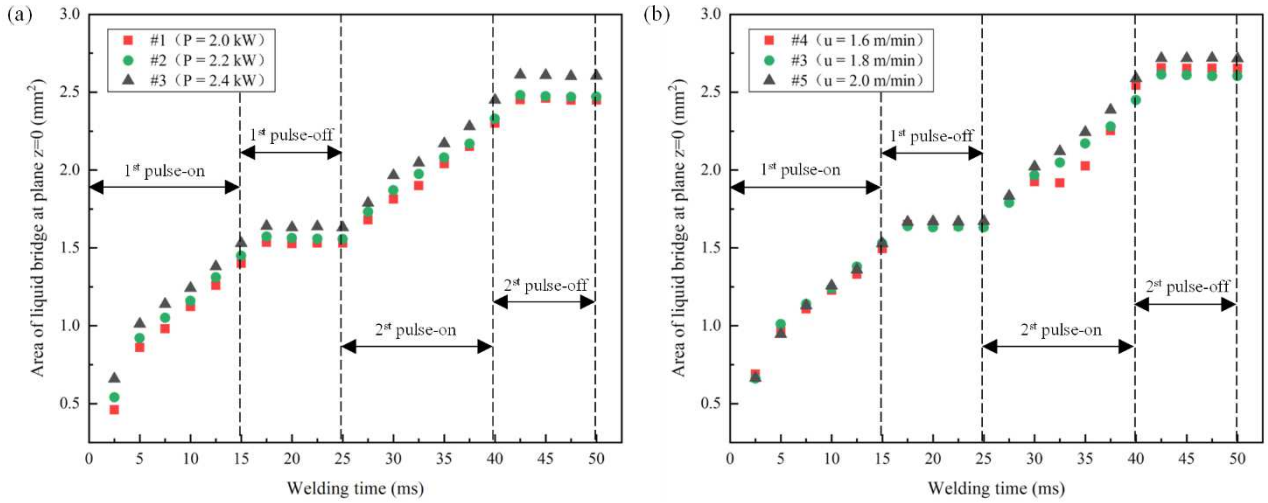

Fig. 14. Variation of liquid bridge area with welding time at z = 0 plane under different heat input conditions: (a) Under different peak laser power; (b) Under different welding speeds.

5. Conclusions

Using the developed multi-physical field CFD model, the dynamic simulation of the PLBW process of Ti6Al4V thin plate with 0.2 mm clearance was performed. At various initial welding stages, the evolution features of the temperature field, velocity field, and liquid bridge profile were examined. Using various welding heat input parameters, the transient temperature field, keyhole size, and liquid bridge area were computed. The effects of peak laser power and welding speed on the dynamic behavior of molten pools in the PLBW process were investigated. The following are the primary conclusions:

(1) With a 0.2 mm clearance, the proposed PLBW technology and process parameters can weld thin plates of Ti6Al4V and produce a well-formed weld. The weld profile simulated by the CFD model is in good agreement with the experimental results, and the deviation is between 0.68% and 7.95%.

(2) The molten pool's velocity field exhibits both molten metal convection and metal vapor eruption. While the flow rate of liquid metal is less than 2.0 m/s, the maximum eruption speed of metal vapor can reach 90.54 m/s. After the laser power reaches the peak value, the metal steam eruption weakens and the obvious Marangoni vortex appears in the molten pool.

(3) The simulated keyhole is always in three stages—the keyhole appears and then transforms into a through-hole over time. The through hole continues to oscillate until the laser power is reduced to zero, at which point the keyhole ultimately shrinks and disappears. The keyhole shape becomes more curved as the laser peak power rises, suggesting that the keyhole oscillation is enhanced.

(4) When the laser initially acts on the thin plate, the larger peak laser power tends to produce more liquid bridges in the clearance, while the influence of welding speed on the initial liquid bridge profile is not obvious. In the second pulse period, with the increase of welding speed, the area of the liquid bridge rises more regularly, indicating that the increase of welding speed enhances the stability of the molten pool.

Acknowledgements The authors gratefully acknowledged the projects funded by the Priority Academic Program Development of Jiangsu Higher Education Institutions (PAPD) and China Postdoctoral Science Foundation No. 2020M671479.

Funding The research is funded by the Priority Academic Program Development of Jiangsu Higher Education Institutions (PAPD) and China Postdoctoral Science Foundation No. 2020M671479.

Declarations

Ethics approval Not applicable.
Consent to participate The authors declare their consent to participate.
Consent for publication The authors declare their consent for publication.
Conflict of interest The authors declare no competing interest.

References

[1] Fabrizia C, Vittorio A, Gaetano C, Francesco C, Vincenzo S (2013) Investigation and Optimization of Laser Welding of Ti-6Al-4V Titanium Alloy Plates. J Manuf Sci Eng 135(6):061012

[2] Auwal ST, Ramesh S, Yusof F, Manladan SM (2018) A review on laser beam welding of titanium alloys. Int J Adv Manuf Technol 97:1071-1098

[3] Gope DK, Kumar U, Chattopadhyaya S, Mandal S (2018) Experimental investigation of pug cutter embedded TIG welding of Ti-6Al-4V titanium alloy. J Mech Sci Technol 32: 2715-2721

[4] Ghaini FM, Hamedi MJ, Torkamany MJ, Sabbaghzadeh J (2007) Weld metal microstructural characteristics in

pulsed Nd: YAG laser welding. Scr Mater 56:955-958

[5] Mohid Z, Rafai NH, Ibrahim MR, Rahim EA (2017) Melted Zone Shapes transformation in titanium alloy welded using pulse wave laser. Mater Sci Forum 882:8-12

[6] Junaid M, Baig MN, M. Shamir, F. N. Khan, K. Rehman, J. Haider (2016) A comparative study of pulsed laser and pulsed TIG welding of Ti-5Al-2.5Sn titanium alloy sheet. J Mater Process Technol 242:24-38

[7] Gao XL, Zhang LJ, Liu J, Zhang JX (2014) Effects of weld cross-section profiles and microstructure on properties of pulsed Nd: YAG laser welding of Ti6Al4V sheet. Int J Adv Manuf Technol 72:895-903

[8] Kumar U, Patel D, Zaffar Z, Gope DK, Chattopadhyaya S, Das AK, Biswal MK (2018) Experimental and numerical investigation of temperature distribution and analysis of mechanical properties during pulsed Nd-YAG laser welding of thin Ti6Al4V alloy. Mater Sci Eng 377:012158

[9] Aalderink BJ, Pathiraj B, Aarts KM (2010) Seam gap bridging of laser based processes for the welding of aluminum sheets for industrial applications. Int J Adv Manuf Technol 48:143-154

[10] Satyanarayana G, Narayana KL, Nageswara BR, Slobodyan MS, Elkin MA, Kiselev AS (2019) Numerical Simulation of the Processes of Formation of a Welded Joint with a Pulsed ND: YAG Laser Welding of ZR – 1%NB Alloy. Thermal Eng 66:210-218

[11] Pang SY, Chen WD, Wang W (2014) A Quantitative Model of Keyhole Instability Induced Porosity in Laser Welding of Titanium Alloy. Metall Mater Trans 45:2808-2818

[12] Drobniak P, Otto A, Vázquez RG, Arias RM, Arias JL (2020) Simulation of keyhole laser welding of stainless steel plates with a gap. Procedia CIRP 94:731-736

[13] Hao HC, Gao JQ, Huang HS (2020) Numerical simulation for dynamic behavior of molten pool in tungsten inert gas welding with reserved gap. J Manuf Processes 58:11-18.

[14] Katayama S, Kawahito Y (2009) Elucidation of phenomena in high power fiber laser welding, development of prevention procedures of welding defects. Proc SPIE 7195:71951R-5

[15] Chang B, Allen C, Blackburn J, Hilton P, Du D (2015) Fluid flow characteristics and porosity behavior in full penetration laser welding of a titanium alloy. Metall Mater Trans B 46:906-918

[16] Lei Z, Wu S, Cao B (2020) Role of thermal fluid dynamics in alloying element distribution and weld porosity in powder feeding-based laser welding of Al alloy. Appl Therm Eng 171:115081

[17] Pang SY, Chen LL, Zhou JX, Yin YJ, Chen T (2011) A three-dimensional sharp interface model for self-consistent keyhole and weld pool dynamics in deep penetration laser welding. J Phys D 44:25301

[18] Chen JC, Ouyang ZP, Du XW, Wei YH (2022) Weld pool dynamics and joining mechanism in pulse wave laser beam welding of Ti-6Al-4V titanium alloy sheets assembled in butt joint with an air gap. Opt Laser Technol 146:107558

[19] Pilliod JE, Puckett EG (2004) Second-order accurate volume-of-fluid algorithms for tracking material interfaces. J Comput Phys 199:465-502

[20] Osher S, Fedkiw R, Piechor K (2004) Level Set Methods and Dynamic Implicit Surfaces. Appl Mech Rev 57:B15-B15

[21] Sussman M., Smereka P, Osher S (1994) A level set approach for computing solutions to incompressible two-phase flow. J Comput Phys 114:146-159

[22] Qian LG, Wei YH, Xiao F (2018) Coupled THINC and level set method: A conservative interface capturing scheme with high-order surface representations. J Comput Phys 373:284-303

[23] Chen JC, Chen XM, Liu XJ, Wei YH (2022) Numerical investigation on keyhole collapsing and rebuilding behavior during pulsed laser beam welding of Ti6Al4V titanium alloy under various pulse frequencies. Appl Phys A 128:

[24] Yang Z, Tao W, Li L, Chen Y, Shi C (2017) Numerical simulation of heat transfer and fluid flow during double-

sided laser beam welding of T-joints for aluminum aircraft fuselage panels. Opt Laser Technol 91:120-129

[25] Li ZX, Rostam K, Panjehpour A, Akbari M, Karimipour A, Rostamis S (2020) Experimental and numerical study of temperature field and molten pool dimensions in dissimilar thickness laser welding of Ti6Al4V alloy. J Manuf Process 49:438-436

[26] Pariona MM, Taques AF, Wojciechowski LA (2018) The Marangoni effect on microstructure properties and morphology of laser-treated Al-Fe alloy with single track by FEM: Varying the laser beam velocity. Int J Heat Mass Tran 119:10-19

[27] Chang B, Allen C, Blackburn J, Hilton P, Du D (2015) Fluid flow characteristics and porosity behavior in full penetration laser welding of a titanium alloy. Metall Mater Trans B 46:906-918

[28] Chen XM, Wei YH, Chang YT, Kong B, Chen JC (2022) Study on keyhole characteristics and weld pool dynamics of Ti6Al4V alloy fabricated by continuous wave laser beam welding. Int J Adv Manuf Technol 119: 2999-3012